



Publication Year	2021
Acceptance in OA @INAF	2021-09-27T07:47:41Z
Title	The Impact of the CMB on the Evolution of high-z Blazars
Authors	Ighina, L.; CACCIANIGA, Alessandro; MORETTI, Alberto; Belladitta, S.; DELLA CECA, Roberto; et al.
DOI	10.1093/mnras/stab1612
Handle	http://hdl.handle.net/20.500.12386/31051
Journal	MONTHLY NOTICES OF THE ROYAL ASTRONOMICAL SOCIETY
Number	505



The impact of the CMB on the evolution of high- z blazars

L. Ighina^{1b},^{1,2}★ A. Caccianiga^{1b},¹ A. Moretti,¹ S. Belladitta,^{1,2} R. Della Ceca¹ and A. Diana^{1b}³

¹INAF, Osservatorio Astronomico di Brera, via Brera 28, I-20121 Milano, Italy

²DiSAT, Università degli Studi dell'Insubria, via Valleggio 11, I-22100 Como, Italy

³Dipartimento di Fisica G. Occhialini, Università degli Studi di Milano-Bicocca, Piazza della Scienza 3, I-20126 Milano, Italy

Accepted 2021 May 31. Received 2021 May 12; in original form 2021 March 22

ABSTRACT

Different works have recently found an increase of the average X-ray-to-radio luminosity ratio with redshift in the blazar population. We evaluate here whether the inverse Compton interaction between the relativistic electrons within the jet and the photons of the cosmic microwave background (IC/CMB) can explain this trend. Moreover, we test whether the IC/CMB model can also be at the origin of the different space density evolutions found in X-ray and radio-selected blazar samples. By considering the best statistically complete samples of blazars selected in the radio or in the X-ray band and covering a large range of redshift ($0.5 \lesssim z \lesssim 5.5$), we evaluate the expected impact of the CMB on the observed X-ray emission on each sample and then we compare these predictions with the observations. We find that this model can satisfactorily explain both the observed trend of the X-ray-to-radio luminosity ratios with redshift and the different cosmological evolutions derived from the radio and X-ray band. Finally, we discuss how currently on-going X-ray missions, like *extended ROentgen Survey with an Imaging Telescope Array*, could help to further constrain the observed evolution at even higher redshifts (up to $z \sim 6$ –7).

Key words: galaxies: active – galaxies: high-redshift – galaxies: jets – galaxies: nuclei – X-rays: galaxies.

1 INTRODUCTION

Blazars are radio-loud (RL¹) active galactic nuclei (AGNs) with a relativistic jet directed close to our line of sight. Because of this particular orientation, the relativistic amplification of the jetted radiation makes blazars extremely bright sources and thus visible even in the primordial Universe, with the most distant currently observed at $z = 6.1$ (Belladitta et al. 2020). Interestingly, from the observation of one of these sources we can infer the total number of RL AGNs at the same redshift with similar properties, but with a misaligned jet: $N_{\text{tot}} \approx N_{\text{obs}} \times 2\Gamma^2$ (e.g. Sbarrato et al. 2015), with Γ the bulk Lorentz factor of the plasma within the jet ($\Gamma \sim 5$ –15, e.g. Ghisellini et al. 2015). Combined, these two features make blazars ideal tools to study the cosmological evolution of supermassive black holes (SMBHs) hosted in RL AGNs and to understand the role that relativistic jets play in their growth.

Studies of X-ray-selected samples of blazars ($2 < z < 4$) found that the space density of the most X-ray luminous flat spectrum radio quasars (FSRQs; hereafter simply blazars²) has a unique cosmological evolution, with a peak at larger redshift ($z \sim 3.5$ –4; Ajello et al. 2009; Toda, Fukazawa & Inoue 2020) compared to the radio-quiet (RQ) population (Hopkins, Richards & Hernquist

2007; Shen et al. 2020), even considering the X-ray brightest RQ AGNs ($z \sim 2.5$, Aird et al. 2015). This result led different authors (Ghisellini et al. 2013; Sbarrato et al. 2015) to suggest that the formation and the growth of the most massive ($M_{\text{BH}} > 10^9 M_{\odot}$) RL AGNs is faster compared to the RQ population with similar masses, implying a strong connection between the jet and the accretion process. However, analogous studies performed on radio-selected samples of blazars found that their density evolution in the radio band is similar to the one observed in the RQ population (Mao et al. 2017; Caccianiga et al. 2019), even when considering the most massive AGNs [$M_{\text{BH}} > 10^9 M_{\odot}$, Diana et al. (in preparation)]. Since in the spectral energy distribution (SED) of blazars both the X-ray and the radio bands are dominated by the emission produced within the relativistic jet, such a discrepancy is not obvious and its understanding is of utmost importance if we want to reliably use blazars as tracers of the SMBHs evolution.

One possible explanation could be that the typical X-ray-to-radio ratio (X/R) increases with redshift. Indeed, such an evolution has been observed at high redshift, first in very radio-powerful AGNs (Wu et al. 2013) and then also in the specific class of blazars (Ighina et al. 2019), where it was found that $z > 4$ blazars have on average X/R ratios ~ 2 times larger than low- z ones ($z \sim 1$). One possibility often invoked in the recent literature that predicts this type of trend is that the increase of the X/R ratios is due to an enhanced X-ray emission caused by the interaction between the relativistic electrons in the jet and the photons of the cosmic microwave background (CMB). In this case, we expect a fraction of the electrons in the extended parts (a few kpc, e.g. Paliya et al. 2020a) of the jet to interact via inverse Compton scattering with the CMB photons (IC/CMB) at any given redshift. Since the CMB energy density grows as $U_{\text{CMB}} \propto (1+z)^4$, this process is expected to become more important at higher

* E-mail: lighina@uninsubria.it

¹We consider a source to be radio loud if it has a radio loudness $R > 10$, where R is defined as the ratio between the 5 GHz and 4400 Å rest-frame flux densities, $R = S_{5\text{GHz}}/S_{4400\text{Å}}$ (Kellermann et al. 1989).

²In this work, we only consider the FSRQ and not the BL Lac class of blazars. Indeed only a few BL Lac sources have been observed at high redshift (e.g. Paliya et al. 2020b).

redshifts and thus to increase the observed X/R ratios. Moreover, this type of X-ray luminosity evolution with redshift would also increase the number of observed blazars in flux-limited X-ray surveys (and thus their space density) in a similar way to what was found by Ajello et al. (2009). Even though other interpretations have been proposed to explain the observed discrepancies (see e.g. Wu et al. 2013), the IC/CMB model has acquired more and more popularity after the launch of the *Chandra* X-ray observatory and the discovery of many extended X-ray jets, even at high redshift (e.g. Tavecchio et al. 2000; Siemiginowska et al. 2007; Napier et al. 2020; Schwartz et al. 2020). Nevertheless, a scenario where all the X-ray and γ -ray extended emission is solely related to an IC/CMB process has been challenged several times by observations in the local Universe (e.g. Georganopoulos et al. 2006; Meyer & Georganopoulos 2014; Breiding et al. 2017), with only two sources having met the IC/CMB predictions (Meyer et al. 2019). Interestingly, both these objects are blazars, suggesting that orientation plays an important role in the observability of the IC/CMB emission (e.g. Simionescu et al. 2016). In any case, we still expect the IC/CMB interaction to take place even at scales not resolved by current X-ray facilities, especially at high z . The real question is the relative amount of X-ray radiation produced through this process with respect to the total one observed. For this reason, a *fractional* IC/CMB model has been recently proposed (Wu et al. 2013), where the interaction with the CMB is responsible for only a small fraction (~ 3 per cent) of the total X-ray emission at low redshift ($z \sim 1$, e.g. Zhu et al. 2019) becoming more and more important at $z > 3$ –4, where it can be dominant.

In this work, by using a statistical approach, we want to verify whether the X-ray enhancement observed in high- z blazars can be explained by a *fractional* IC/CMB model and if this same type of evolution can also explain the differences observed in the space density of blazars obtained from X-ray and radio surveys.

The paper is structured as follows: in Section 2, we present the blazar samples and relative data used throughout the work; in Section 3, we discuss the expected X/R ratios evolution considering an IC/CMB scenario and how it compares to observations; in Section 4, we derive the expected X-ray space density evolution from the IC/CMB model and compare it with observations; in Section 5, we show how this model can be tested with currently on-going X-ray missions; finally, in Section 6 we summarize our results and conclusions.

We assume a flat Λ CDM cosmology with $H_0 = 70 \text{ km s}^{-1} \text{ Mpc}^{-1}$, $\Omega_m = 0.3$, and $\Omega_\Lambda = 0.7$. Spectral indices are given assuming $S_\nu \propto \nu^{-\alpha}$ and all errors are reported at 1σ , unless otherwise specified.

2 BLAZAR SAMPLES

In order to study the evolution of blazars across cosmic times in this work, we considered three different blazar samples that, together, cover an extended range of redshifts, from the local Universe, $z \sim 0.5$, up to $z \sim 5.5$. A full description of the first two samples (C19 and BZ1.5Jy) is given in Caccianiga et al. (2019) and Ighina et al. (2019), respectively, here we report only a short summary of them.

(i) **C19 sample:** It is the largest flux-limited ($S_{5 \text{ GHz}} > 30 \text{ mJy}$) sample of blazars at $z > 4$. The sources have been selected from the Cosmic Lens All Sky Survey (CLASS; Myers et al. 2003) in the radio band and then followed up spectroscopically (Caccianiga et al. 2019) in order to have a confirmation of their high- z nature. After completing the X-ray coverage of the sample through dedicated observations we analysed their X-ray properties and identified the

bona fide blazars accordingly (Ighina et al. 2019).³ The final sample is composed by 22 objects (over a total of 25 candidates) with mean redshift $z \sim 4.5$.

(ii) **BZ1.5Jy sample:** In order to have a reference sample at lower redshift and in the same range of radio luminosities of the C19 one, we considered all the blazars FSRQs in the 5th edition of the BZCAT catalogue (Massaro et al. 2015) with a radio flux density $S_{1.4 \text{ GHz}} > 1.5 \text{ Jy}$. At these high flux density levels almost all blazars have been discovered and identified and thus this can be confidently considered as a radio flux limited sample with radio luminosities similar to the C19 sample. Moreover, with such an high-flux limit the large majority of these objects has already been observed (and detected) in the X-rays, thus avoiding any possible bias against X-ray weak blazars. Finally, we considered the ones observed by the *Swift*–XRT telescope, which have radio properties similar to the rest of the sources, and analysed their X-ray spectra. There are a total of 46 sources in this sample, with mean redshift $z \sim 1.1$;

(iii) **BAT105 sample:** The sources of this sample were selected from *The 105-Month Swift*–BAT All-sky Hard X-Ray Survey catalogue (Oh et al. 2018), which is the collection of all the *Swift*–BAT observations (in the 14–195 keV band) during its first 105 months of activity. Since we are interested in the X-ray properties of high redshift blazars, we started by considering only the sources with $z > 2$. We then selected all the objects with an X-ray flux $f_{14-195 \text{ keV}} > 8.40 \times 10^{-12} \text{ erg s}^{-1} \text{ cm}^{-2}$, above which the sky coverage can be considered approximately constant (see fig. 11 in Oh et al. 2018) and the catalogue complete over 90 per cent of the entire sky. Then, in order to select all the bona fide blazars we considered all the objects with a radio counterpart in the NRAO VLA Sky Survey (NVSS; Condon et al. 1998). We note that adopting this approach we are also including two sources (SWIFT J0909.0 + 0358 at $z = 3.288$ and SWIFT J0131.5–1007 at $z = 3.515$) that are not classified as blazars in the BAT catalogue, but which, after its publication, were identified as such (Paliya et al. 2019; Marcotulli et al. 2020) according to their broad-band properties. In the following, we will also consider the soft X-ray (0.3–10 keV) properties of these sources as reported in the second version of the *Swift*–XRT Point Source catalogue (2SXPS; Evans et al. 2020). In total there are 20 objects in this sample, with a mean redshift of $z \sim 2.9$.

In Fig. 1, we show the X-ray (2–10 keV) and radio (1.4 GHz) rest-frame luminosity distributions together with the mean X-ray-to-radio luminosity ratio ($X/R = \log \frac{L_{2-10 \text{ keV}}}{L_{1.4 \text{ GHz}}}$) for each of the three samples described above. From the plot, it is clear that the three samples have on average significantly different ratios. We note that both the X-ray and radio luminosities refer to the indicated rest-frame frequencies (i.e. they have been k -corrected). In order to compute the rest-frame X-ray luminosities we adopted the photon index measured in the 0.3–10 keV observation of each object, which also covers the 2–10 keV rest-frame band in the redshift range here considered, $z = 0$ –5.5. In the radio band we used the observed spectral index for the C19 sample (0.15–1.4 GHz, Caccianiga et al. 2019), while we assumed a flat spectral index ($\alpha_r = 0$), which is typical of FSRQs (Padovani et al. 2017), for the BZ1.5Jy and the BAT105 samples. We note that by adopting a flat radio spectrum also for the entire C19 sample, their X/R ratios distribution does not significantly change (the shift in the mean value is < 0.05). For these reasons, the X-ray and radio

³We note that the last blazar (GB6J1711 + 3830) was observed and classified as such after the publication of Ighina et al. (2019) therefore we report in Appendix A the analysis of its *Swift*–XRT observation.

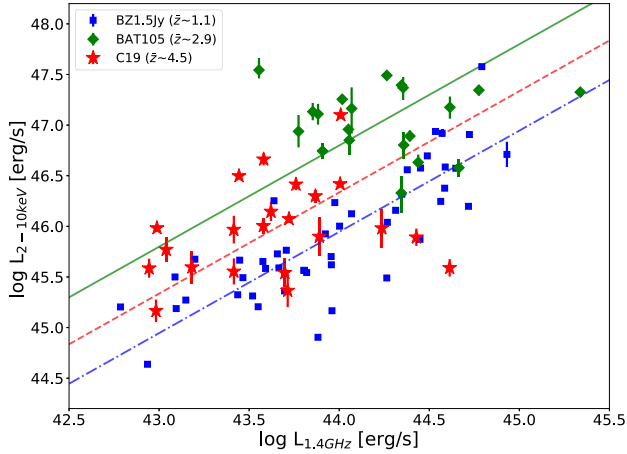


Figure 1. X-ray luminosity in the 2–10 keV energy band as a function of the radio luminosity at 1.4 GHz. The sources are represented with different symbols according to the sample they belong to: the blue squares = BZ1.5Jy, the red stars = C19, and the green diamonds = BAT105. Beside the name of each sample in the legend, we also report the mean redshift of each sample in brackets. The errors on the X-ray luminosities are at 90 percent confidence level. The three lines represent the mean X-ray-to-radio luminosity ratio of the given sample: dash-dotted blue for BZ1.5Jy, $\langle \log(L_X/L_R) \rangle = 1.95$; dashed red for the C19, $\langle \log(L_X/L_R) \rangle = 2.34$; and solid green for BAT105, $\langle \log(L_X/L_R) \rangle = 2.80$.

slopes can be considered relatively well constrained and therefore the observed discrepancy in the X/R ratios at low and high z cannot be attributed to a different redshift-dependent sampling of the rest-frame spectra. In the following, we will test whether the observed evolution in the X/R values can be explained by the interaction of the relativistic jets with the photons from the CMB.

3 REDSHIFT EVOLUTION OF THE X-RAY-TO-RADIO LUMINOSITY RATIOS

3.1 IC/CMB expected trend

As previously mentioned, different independent studies of the most powerful RL AGN population (i.e. mostly blazars) found a similar increase of the X-ray emission as a function of redshift when compared to both the optical emission (e.g. Wu et al. 2013; Zhu et al. 2019) and the radio one (e.g. McKeough et al. 2016; Ighina et al. 2019). In this work, we want to verify whether the observed evolution can be explained as due to a *fractional* IC/CMB interaction by focusing on well-defined samples of blazars. According to this model, only a small fraction of the total X-ray luminosity is produced via the IC/CMB mechanism, which, however, largely depends on redshift since it follows the CMB energy density trend, $U_{\text{CMB}} \propto (1+z)^4$. At the same time we are also expecting an analogous decrease of the radio emission produced by the same electrons, which are quickly cooled down by the IC interaction with the CMB (e.g. Schwartz et al. 2019). However, this kind of effect can be considered negligible in the blazar class, since their observed radio emission at high frequencies is dominated by the beamed photons produced in the compact innermost region of the jet, close to the accreting SMBH (e.g. Ghisellini & Tavecchio 2009), where the extremely large magnetic field energy density overpowers the CMB one even at high redshift (e.g. Afonso et al. 2015). Therefore, while the overall radio emission can be considered to remain unchanged with respect to redshift, the fraction of X-ray emission produced through an IC/CMB

interaction will become more relevant or even dominant at high z , even if it is negligible at low redshift. According to this model, the overall X-ray-to-radio luminosity ratio of blazars can be expressed as

$$\frac{L_X}{L_R}(z) = \frac{L_X}{L_R}(z=0) \times [(1 - A_0) + A_0(1+z)^4], \quad (1)$$

where A_0 represents the fraction of the X-ray emission produced by the interaction with CMB photons at $z = 0$. In the following, we consider the X-ray luminosity integrated in the 2–10 keV band, while the radio one at 1.4 GHz, unless otherwise specified.

In order to explain the observed difference between the low- z and high- z X/R ratios, the fraction of X-ray luminosity produced by the IC/CMB interaction at $z = 0$, should be, as expected, very small on average: $A_0 \approx 0.0016$ (Ighina et al. 2019), but the corresponding amplification factor $(1 - A_0 + A_0(1+z)^4)$ would be ~ 2 at $z \sim 4$.

Moreover, even though we can expect the overall population to follow on average the redshift trend predicted by the IC/CMB model, the importance of this interaction may vary from source to source depending on the physical properties of each SMBH and jet, and thus resulting in a scatter around the mean relation (e.g. Cheung 2004). Indeed, as shown in Fig. 1, a large scatter around the mean X/R values is present also in all the three samples considered here. For this reason, we improved the analysis of the previous work by assuming that the impact of the CMB interaction is not the same for all sources, but, instead, it follows a distribution of values that we derived from observations. As we will see below the assessment of this scatter is necessary to understand the extreme features observed in the BAT105 sample.

3.2 Comparison with observations

In order to determine the redshift evolution of the X/R ratios, we started by assuming that both the initial X/R values at $z = 0$ and the A_0 parameter follow a lognormal distribution. The first is constrained by the observed X/R values at $z \sim 1$, in the BZ1.5Jy sample⁴ ($\langle X/R \rangle = 1.95$ and $\sigma_{X/R} = 0.35$). In order to estimate the best distribution describing the A_0 parameter, we computed the expected X/R values at $z = 4.5$ (mean redshift of the C19 sample) from equation (1) for different $\langle \log A_0 \rangle$ and $\sigma_{\log A_0}$. Comparing the expected distributions with the values observed in the C19 sample through the Kolmogorov–Smirnov (KS; Smirnov 1948) test we found that the best parameter set is given by $\langle \log A_0 \rangle = -2.74$ and $\sigma_{\log A_0} = 0.66$ (KS p-value = 0.84). The two theoretical X/R distributions just described are reported in Fig. 2 (left-hand panel) together with the ones actually observed in the BZ1.5Jy and C19 samples. It is interesting to note that in the case of $\sigma_{\log A_0} = 0$ we have $A_0 \approx 0.002$, similar to the one estimated in Ighina et al. (2019) where we had assumed a single value of A_0 instead of a distribution. In Fig. 3, we report the expected X/R evolution for a radio-selected sample of blazars as a function of redshift considering the distribution of initial values observed in the BZ1.5Jy and the best-fitting $\log A_0$. The evolution of sources having an initial X/R ratio and $\log A_0$ parameter both within 1σ and 2σ from the central values is highlighted (the yellow regions and the black-dashed lines). We also report the X/R values for the sources in the three samples here considered as a function of their redshift, together with other confirmed blazars at $z > 2$ from the literature.

While the mean redshift of the BAT105 sample is $z \sim 3$, its X/R mean value is higher compared to the C19 sample at $z \sim$

⁴This is valid if A_0 is, as expected, very small. Condition that we have checked a posteriori.

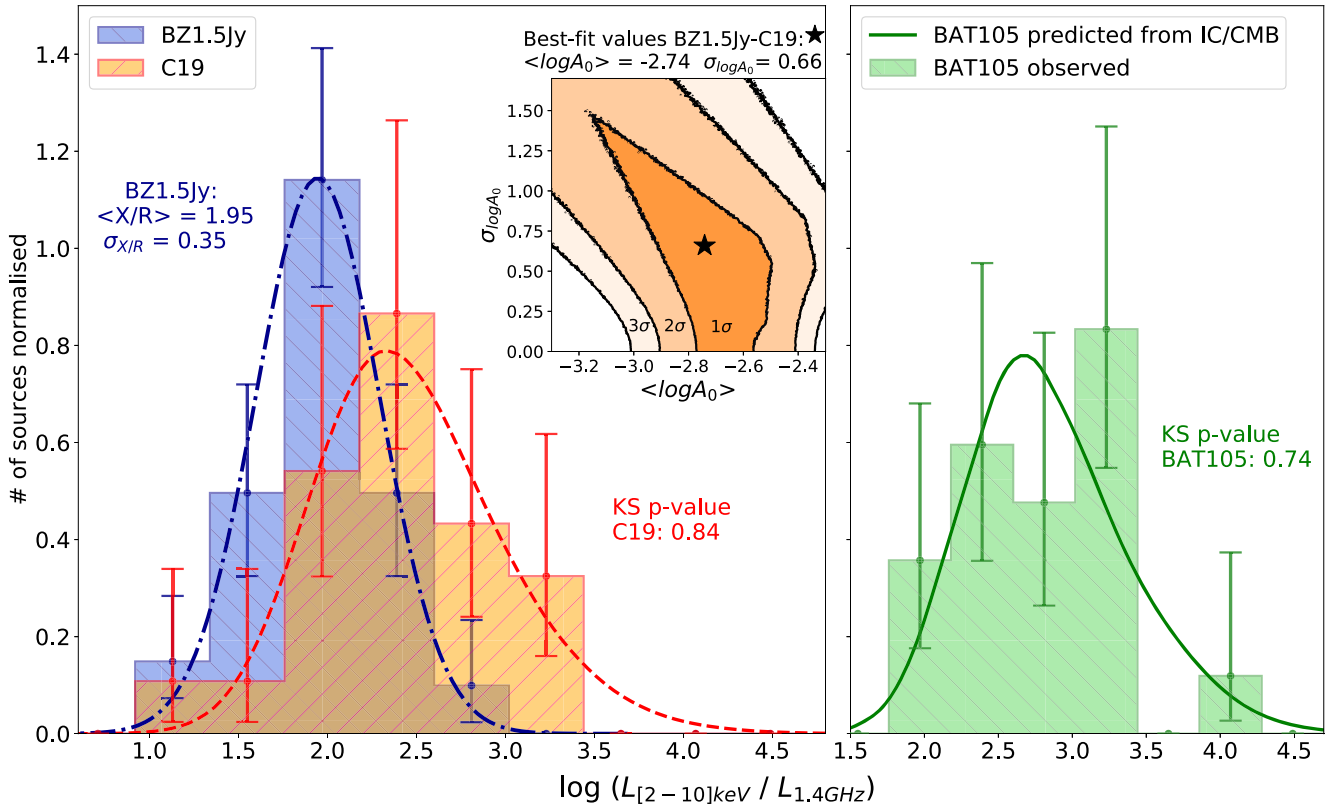


Figure 2. **Left-hand panel:** observed X/R distributions used to derive the $\langle \log A_0 \rangle$ and $\sigma_{\log A_0}$ parameters: the BZ1.5Jy sample (the blue-filled histogram) with its best-fitting lognormal distribution (the dash-dotted blue line) and the C19 sample (the filled orange histogram) with its best-fitting X/R distribution computed from equation (1) at $z = 4.5$ (the red-dashed line). In the top right corner we report the 1σ , 2σ , and 3σ confidence contours for the $\langle \log A_0 \rangle$ and $\sigma_{\log A_0}$ parameters obtained from the comparison between the IC/CMB model and the X/R ratios distribution in the C19 sample. The best-fitting parameter is shown with a black star. **Right-hand panel:** comparison between the observed (the green-filled histogram) X/R distributions for the *Swift*–BAT survey at $2 < z < 5$ and the expected one (the solid green line) considering an IC/CMB model with the parameters derived from the samples in the left-hand panel. We stress that the green curve is not a fit to the BAT data but it is the prediction of the model described in the text. The error-bars indicate the Poisson errors associated to each bin of the distributions.

4.5. Indeed, it is clear from Fig. 3 that the BAT105 sample is largely composed by sources where both the initial X/R and the A_0 values are $>1\sigma$ far from the mean ones. This is likely a selection bias which favours the inclusion of the extreme X-ray sources. In order to quantitatively test this hypothesis, we started from the radio luminosity function (RLF) derived by Mao et al. 2017 (hereafter Mao17)⁵ by creating a mock sample where redshift and radio flux/luminosity are known for each source. We then considered the X/R distribution predicted by the IC/CMB model (using the best-fitting values derived above) at the redshift of each source to estimate their X-ray luminosity. In particular, for each simulated object at redshift z , we randomly extracted an X/R value from the predicted distribution at that redshift and then computed the corresponding X-ray luminosity given the radio luminosity of the source. In order to convert the X-ray luminosity from the 2–10 keV into the 14–195 keV and to compute the corresponding observed flux, we assumed a photon index $\Gamma = 1.54$. This is the mean value obtained in Ricci et al. (2017) by analysing the broad-band XRT–BAT spectra (0.3–150 keV, observed frame) of all the FSRQs in the 70 month *Swift*–BAT catalogue (Baumgartner et al. 2013). Finally, we apply to

the mock sample the same X-ray flux limit of the BAT105 sample: $f_{14-195 \text{ keV}} > 8.40 \times 10^{-12} \text{ erg cm}^{-2} \text{ s}^{-1}$. In Fig. 2 (right-hand panel), we show the BAT105 sources (the green-filled histogram) together with the simulated sample generated as explained above (the solid green line).

By comparing the predicted and observed distribution for X-ray-selected samples with the KS test we found that an IC/CMB model, with the parameters fixed to those that best explain the X/R observed in the C19 sample, naturally predicts the presence of objects with extreme X-ray properties already at $z \sim 3$, as actually observed in BAT105 (KS p-value = 0.74). We note that if we had instead assumed a constant X/R conversion given by the distribution observed at $z \sim 1$, the expected and observed distributions in BAT105 would have been inconsistent (KS p-value $< 10^{-4}$).

4 SPACE DENSITIES: RADIO VERSUS X-RAY

As already mentioned, X-ray and radio-selected samples of blazars seem to find a different evolution, with radio-selected blazars peaking at $z \sim 2$ (Mao17), similar to the RQ population, and X-ray selected ones at about $z \sim 4$ (Ajello et al. 2009, hereafter Aj09). We now want to update the Aj09 results, using the most recent version of the *Swift*–BAT sample, and to compare them with the predictions based on the model described in the previous section.

⁵Computed using a sample of radio-selected blazars at 1.4 GHz in the range $z = 0.5-3$. In this work, we considered the RLF derived from the ‘clean sample’ discussed in Mao17.

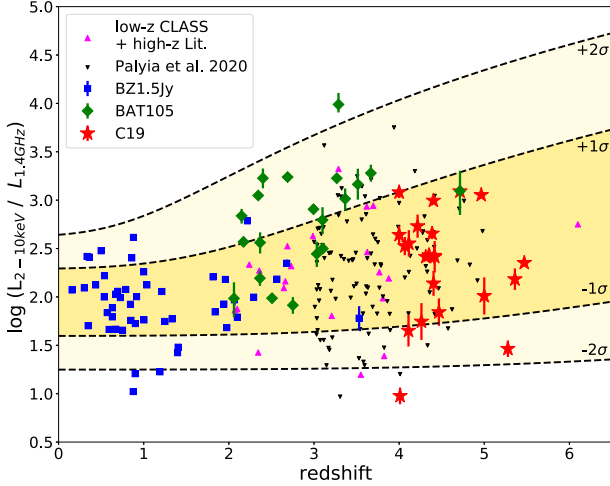


Figure 3. Expected evolution of the overall X/R ratios as a function of redshift for a radio-selected sample of blazars considering an initial distribution with $\langle X/R \rangle = 1.95$, $\sigma_{X/R} = 0.35$, and a distribution for the $\log A_0$ parameter described by $\langle \log A_0 \rangle = -2.74$ and $\sigma_{\log A_0} = 0.66$. The black-dashed lines represent the expected evolution for a source with both the initial X/R and $\log A_0$ distant 1σ or 2σ from the mean values. The different data points represent the samples the sources belong to BZ1.5Jy (the blue squares), BAT105 (the green diamonds), and C19 (the red stars). We also report $z > 2$ blazars taken from the literature: the magenta triangles are $2 < z < 4$ blazars from the CLASS survey that were serendipitously observed by the *XMM-Newton* or *Swift*-XRT telescopes plus the only $z > 6$ confirmed blazars (Belladitta et al. 2020); the black triangles are bona fide blazars discussed in Paliya et al. (2020a).

4.1 The blazar space density evolution from the 105-months BAT sample

The Aj09 work was based on an old version of the BAT catalogue (36 months) therefore we decided to update the analysis using the most recent version that now includes data from the 105-months BAT catalogue (Oh et al. 2018). Since the particular evolution has been observed in the most X-ray luminous blazars, $\log L_{15-55 \text{ keV}} > 47.3 \text{ erg s}^{-1}$ (Aj09), we consider the same population of sources, that is, $\log L_{14-195 \text{ keV}} > 47.7 \text{ erg s}^{-1}$ (where we assumed again $\Gamma = 1.54$ for the conversion between the two bands) corresponding to 18 sources of the 20 in the initial sample. Moreover, given the limiting flux of the BAT105 sample, we should be able to observe the majority of the sources within this luminosity range and with a photon index around 1.5 up to $z \sim 4.5$. With this BAT105 sub-sample, we estimated the space density of blazars in the redshift range $z = 2-5$ using the V_{max} method (Schmidt 1968). After dividing the redshift range in three bins, each containing at least three sources, we computed the space density in each of them as follows:

$$\rho(z_1, z_2) = \frac{1}{f_{\text{sky}}} \times \sum \frac{1}{V_{\text{max}}}, \quad (2)$$

where f_{sky} is the fraction of the sky here considered ($= 0.74$) and the sum is on the objects within the redshift bin z_1-z_2 , while V_{max} is the co-moving volume within which each source could have been observed. In other words, V_{max} is the co-moving volume between z_1 and the minimum between z_2 and the redshift at which the X-ray flux of the given source corresponds to the limit of the sample. The errors on each density estimate is then given by $\frac{\sigma_P}{N} \times \rho(z_1, z_2)$, where N is the number of objects in the given redshift bin and σ_P the Poisson uncertainty on N .

Table 1. X-ray space density of blazars with $\log L_{14-195 \text{ keV}} > 47.7 \text{ erg s}^{-1}$ from the BAT105 sample. The values are also shown in Fig. 4 (the green squares).

Redshift bin	$2 < z < 2.75$	$2.75 < z < 3.5$	$3.5 < z < 4.8$
$\log \rho \text{ (Gpc}^{-3}\text{)}$	$-1.58^{+0.19}_{-0.20}$	$-1.51^{+0.17}_{-0.18}$	$-1.83^{+0.29}_{-0.34}$
Number of sources	7	8	3

In order to account for the unidentified sources (i.e. without an associated redshift) in the BAT catalogue and the possibility that one or more of them are actually $z > 2$ blazars, we proceeded as follows. We applied to these objects the same criteria used to build the BAT105 sample, i.e. an X-ray flux above the completeness limit and a counterpart in the NVSS (see Section 2). We then searched for possible identifications of the remaining sources in the recent literature, finding that the majority of them have been followed up with dedicated spectroscopic observations within the *BAT AGN Spectroscopic Survey* project (Koss et al. 2017) and turned out to be low- z objects. Among the still unidentified sources (~ 20), only three of them have similar properties compared to the blazars here considered, namely a radio flux density $S_\nu > 100 \text{ mJy}$. Since we cannot exclude that these three sources are in fact $z > 2$ blazars, we assumed them to have the same redshift distribution as the BAT105 objects with a similar radio flux. In particular, we computed the probability that one source has to belong to one of the different redshift bins here considered and then we increased the corresponding number of objects by this fraction times the number of possible blazars (3). We report the values obtained in Table 1, and we show the space density evolution in Fig. 4 (the green squares) together with the estimates of Aj09 (the blue points) as a reference. Interestingly, by sampling a larger co-moving volume and redshift range compared to Aj09 (up to $z \sim 4.5$, i.e. where the peak in Aj09 was expected), we found that the X-ray evolution is not as extreme as previously thought, with the space density peaking at redshift lower than 3.5 (the actual value of the peak is hard to constrain given the limited size of the sample). However, as explained in the next subsection, we still find a discrepancy with respect to the space densities derived from radio surveys.

4.2 Comparing X-ray and radio results

In order to compare the X-ray space density computed few lines above to the one derived from radio observations, we considered once again the RLF determined by Mao17. Assuming a constant X/R conversion factor such as the one observed in the BZ1.5Jy sample ($\bar{z} \sim 1.1$), we converted the RLF to an X-ray LF (XLF), which can be expressed in terms of the radio one as follows:

$$\Phi_X(L_X, z) \times L_X = \Phi_R(L_R, z) \times L_R, \quad (3)$$

where, in this case, L_X indicates the luminosity in the 14–195 keV energy band. Since the X-ray luminosities used to compute the X/R ratios for the C19 and the BZ1.5Jy samples are measured in the 2–10 keV energy range, we assumed again a conversion factor associated to a photon index $\Gamma = 1.54$. As shown in Fig. 4 (the blue-dashed line), in this case the expected number of blazars is significant smaller compared to the estimates from the BAT105 sample, with the space density differing by a factor of ~ 2 (6) at $z \sim 2.3$ (4.2).

In order to verify if the interaction with the CMB could reconcile the two space density evolutions, when computing the XLF in equation (3) we also considered radio-to-X-ray conversion factors given by equation (1) where the parameter A_0 follows the best-fitting

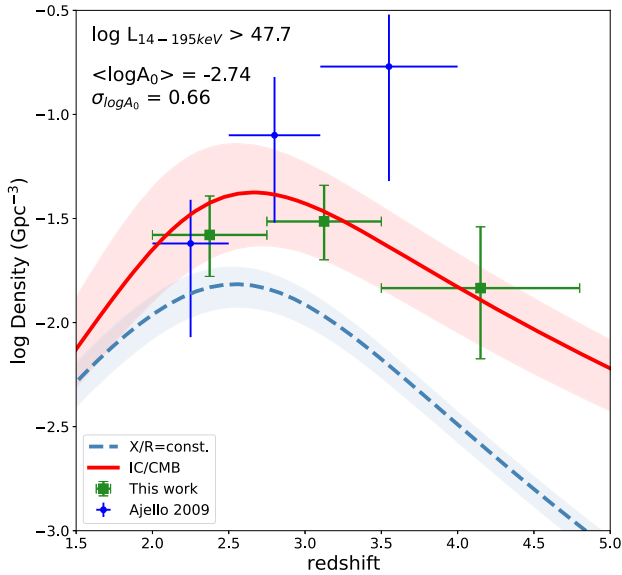


Figure 4. Evolution of the X-ray space density of blazars as a function of redshift. The green squares are the space density obtained from the blazars in the 105-months BAT catalogue, while the space density computed by Ajello using the 36-months BAT catalogue is reported with the blue points. We also show the expected space density computed from the RLF discussed in Mao17 assuming both a constant X/R conversion factor (observed in the BZ1.5Jy, $\langle X/R \rangle = 1.95$, $\sigma_{X/R} = 0.35$, the blue-dashed line) and a redshift evolving one that follows the trend predicted by the IC/CMB model derived in Section 3 (with parameters: $\langle \log A_0 \rangle = -2.74$ and $\sigma_{\log A_0} = 0.66$, the solid red line). The shaded areas represent the variation of the expected space densities assuming a different photon index ($\Gamma = 1.5\text{--}1.6$) and $\langle \log A_0 \rangle$, $\sigma_{\log A_0}$ parameters (with a p-value > 0.7).

distribution obtained in the previous section. We report in Fig. 4 the X-ray space density obtained from the integration of the XLF considering the effect of CMB (the solid red line). The shaded areas show the expected evolutions assuming a different photon index (Γ in the range 1.5–1.6, the median values observed at energies 20–100 keV in a radio-selected sample of blazars, Langejahn et al. 2020) and a different distribution of the $\log A_0$ parameter that can still well reproduce the observed C19 X/R ratios (p-value > 0.7 , see Section 3). As it is clear from Fig. 4, the effect of the CMB derived from the properties of $z > 4$ radio-selected blazars seems to be able to reconcile the cosmological evolutions observed in the radio and in the X-ray bands by increasing the expected space density of X-ray-selected blazars, especially at high redshift. It is worth noting that the IC/CMB model does not predict a significant shift of the space density peak computed from X-ray surveys, but only a slower decrease after the peak moving towards higher redshift due to the additional X-ray emission coming from the interaction with the CMB photons. As shown above, this is in agreement with our new analysis of the latest BAT data set. Larger X-ray-selected samples able to better constrain the peak, as described in the next section, will be instrumental to test this critical prediction.

5 PREDICTIONS FOR THE EROSITA MISSION

An important observational consequence of the IC/CMB model is the presence of many X-ray powerful blazars at high redshifts. Therefore, one way to further test this scenario is to focus on very high redshift ($z > 4$) blazars, where the effect related to the CMB is

expected to be dominant. To date the most suitable X-ray survey to build a statistically relevant sample of high- z blazars is the *extended ROentgen Survey with an Imaging Telescope Array* (eROSITA; Merloni et al. 2012). Having the maximal sky coverage possible and a relatively high sensitivity (from 4.4×10^{-14} erg s $^{-1}$ cm $^{-2}$ after the first scan, eRASS:1, to 1.1×10^{-14} erg s $^{-1}$ cm $^{-2}$ after eight scans, eRASS:8, in the 0.5–2 keV energy band) this mission is ideal for the detection of a large number of X-ray powerful sources at high- z (e.g. Medvedev et al. 2020; Khorunzhev et al. 2021; Wolf et al. 2021). Following the approach outlined in Section 3 for the BAT105 sample, we computed the number and properties of the blazars expected to be found by the eROSITA mission. As shown in Fig. 5 (left-hand side), the potential number of observed blazars at $z > 4$ is significantly different in an IC/CMB scenario (with the parameters discussed in the previous sections) or in the case the X/R ratios do not evolve with redshift. In particular, if the IC/CMB interaction plays a significant role in the X/R ratios evolution with redshift, we expect to detect about three times more blazars above the eROSITA flux limit compared to a non-evolving scenario (~ 100 versus ~ 40 sources in the final eRASS:8). Another important difference between the two scenarios is that, according to an IC/CMB evolution, we are also expecting to find more blazars in the so-called epoch of re-ionization ($z \gtrsim 6$) where only one blazar has been discovered thus far (Belladitta et al. 2020). Moreover, also the X-ray and radio properties of the detected blazars will be instrumental to check whether their X/R ratios evolve according to the IC/CMB scenario or not. As shown in Fig. 5 (right-hand panel), we expect to observe significantly different values of X/R ratios in the IC/CMB case, with a large number of sources with very extreme X/R values (> 3). Detailed studies on these extreme sources, such as the ones performed on the extended jets of X-ray-bright sources at intermediate redshifts ($z \sim 3$, e.g. Worrall et al. 2020) with the *Chandra* telescope, will be instrumental to further constrain the IC/CMB mechanism.

6 CONCLUSIONS

In this work, we tested whether the recently observed increase of the X/R ratios in high- z blazars (Ighina et al. 2019) can be attributed to a *fractional* interaction between the relativistic electrons in the jet with the CMB photons. We found that, by assuming an intrinsic scatter around the average expected trend (meant to represent the different physical properties of the blazar population), we can reproduce the X/R distributions observed at different redshifts, including the extreme values of the $z > 2$ blazars detected by the *Swift*–BAT X-ray telescope. Moreover, after estimating the X-ray space density evolution of blazars from the latest version of the BAT catalogue (105 months), we found that the same IC/CMB model could also explain the differences between X-ray and radio evolutions of the blazar population reported in the literature (Ajello et al. 2009; Mao et al. 2017). Nevertheless, we cannot exclude that this variation may be related to a different effect, like a significant change in the host galaxy properties with z , for instance (Wu et al. 2013), or even a combination of different effects.

Another crucial way to test and constrain the importance of the IC/CMB interaction will be to focus on the numerous sources at high redshift expected to be found in wide-area X-ray surveys such as those carried out with the eROSITA mission. High angular resolution observations on the most extreme sources with the *Chandra* telescope will be another important and complementary way to constrain the IC/CMB interaction (e.g. Simionescu et al. 2016; Worrall et al. 2020). The systematic study of extended X-ray emission in these

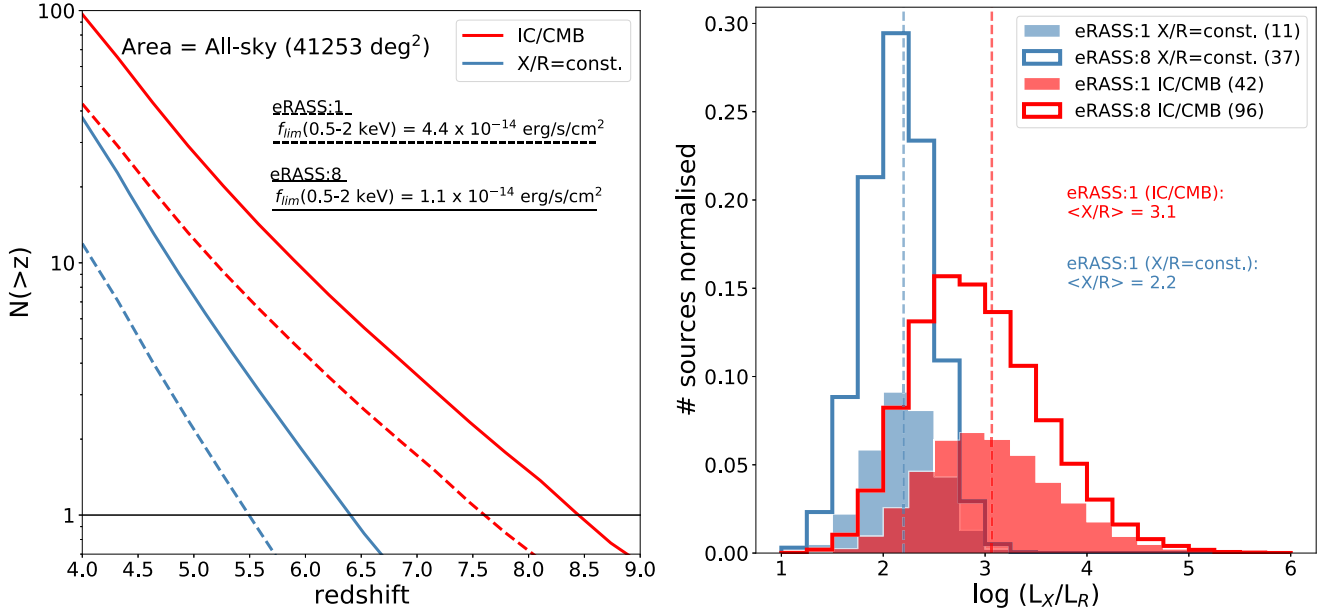


Figure 5. Prediction of the number (left-hand panel) and properties (right-hand panel) of $z > 4$ blazars expected to be found with the eROSITA all-sky survey. In both panels, the red lines represent the estimates made considering the IC/CMB model, whereas the blue lines indicate the estimates assuming non-evolving X/R ratios. The dashed lines and the filled histograms refer to the predictions after the first scan of the sky (eRASS:1), while the continuous lines and the empty histograms are for eight scans (eRASS:8). **Left:** Expected number of detected blazars above a given redshift as a function of redshift. **Right:** X-ray-to-radio ratio distributions. The dashed vertical lines indicate the mean values expected in the eRASS:1. Both the filled and empty histograms have been normalized dividing by the total number of blazars expected in the eRASS:8 considering the corresponding evolving scenario. In the legend, the total number of blazars expected to be observed for each scenario is reported in brackets.

high- z blazars will represent the final confirmation of the relevance of the IC/CMB mechanism on the X-ray emission of high-redshift AGNs.

ACKNOWLEDGEMENTS

We want to thank Massimo Dotti for his help in the last couple of years. We also want to thank Gabriele Ghisellini and Lea Marcotulli for helpful discussions and the referee for their useful comments. We acknowledge financial contribution from the agreement ASI-INAF n. I/037/12/0 and n.2017-14-H.0 and from INAF under PRIN SKA/CTA FORECaST. This work used data supplied by the UK *Swift* Science Data Centre at the University of Leicester. This research used ASTROPY, a community-developed core PYTHON package for Astronomy (Astropy Collaboration 2018).

DATA AVAILABILITY

The majority of the data used in the paper are publicly available as described in the main text. Reprocessed data are available upon request to the main author.

REFERENCES

- Afonso J., Casanellas J., Prandoni I., Jarvis M., Lorenzoni S., Magliocchetti M., Seymour N., 2015, *Advancing Astrophysics with the Square Kilometre Array (AASKA14)*, preprint (arXiv:1412.6040)
Aird J., Coil A. L., Georgakakis A., Nandra K., Barro G., Pérez-González P. G., 2015, *MNRAS*, 451, 1892
Ajello M. et al., 2009, *ApJ*, 699, 603 (Aj09)

- Astropy Collaboration, 2018, *AJ*, 156, 123
Baumgartner W. H., Tueller J., Markwardt C. B., Skinner G. K., Barthelmy S., Mushotzky R. F., Evans P. A., Gehrels N., 2013, *ApJS*, 207, 19
Belladitta S. et al., 2020, *A&A*, 635, L7
Breiding P., Meyer E. T., Georganopoulos M., Keenan M. E., DeNigris N. S., Hewitt J., 2017, *ApJ*, 849, 95
Caccianiga A. et al., 2019, *MNRAS*, 484, 204
Chambers K. C. et al., 2016, preprint (arXiv:1612.05560)
Cheung C. C., 2004, *ApJ*, 600, L23
Condon J. J., Cotton W. D., Greisen E. W., Yin Q. F., Perley R. A., Taylor G. B., Broderick J. J., 1998, *AJ*, 115, 1693
Evans P. A. et al., 2020, *ApJS*, 247, 54
Georganopoulos M., Perlman E. S., Kazanas D., McEnery J., 2006, *ApJ*, 653, L5
Ghisellini G., Tavecchio F., 2009, *MNRAS*, 397, 985
Ghisellini G., Haardt F., Della Ceca R., Volonteri M., Sbarrato T., 2013, *MNRAS*, 432, 2818
Ghisellini G., Tagliaferri G., Sbarrato T., Gehrels N., 2015, *MNRAS*, 450, L34
Gregory P. C., Scott W. K., Douglas K., Condon J. J., 1996, *ApJ*, 103, 427
HIPI Collaboration, 2016, *A&A*, 594, A116
Hopkins P. F., Richards G. T., Hernquist L., 2007, *ApJ*, 654, 731
Ighina L., Caccianiga A., Moretti A., Belladitta S., Della Ceca R., Ballo L., Dallacasa D., 2019, *MNRAS*, 489, 2732
Intema H. T., Jagannathan P., Mooley K. P., Frail D. A., 2017, *A&A*, 598, A78
Kellermann K. I., Sramek R., Schmidt M., Shaffer D. B., Green R., 1989, *AJ*, 98, 1195
Khorunzhev G. A. et al., 2021, preprint (arXiv:2104.05142)
Koss M. et al., 2017, *ApJ*, 850, 74
Langejahn M. et al., 2020, *A&A*, 637, A55

- Mao P., Urry C. M., Marchesini E., Landoni M., Massaro F., Ajello M., 2017, *ApJ*, 842, 87 (Mao17)
- Marcotulli L. et al., 2020, *ApJ*, 889, 164
- Massaro E., Maselli A., Leto C., Marchegiani P., Perri M., Giommi P., Piranomonte S., 2015, *Astrophys. Space Sci.*, 357, 75
- McKeough K. et al., 2016, *ApJ*, 833, 123
- Medvedev P. et al., 2020, *MNRAS*, 497, 1842
- Merloni A. et al., 2012, preprint (arXiv:1209.3114)
- Meyer E. T., Georganopoulos M., 2014, *ApJ*, 780, L27
- Meyer E. T., Iyer A. R., Reddy K., Georganopoulos M., Breiding P., Keenan M., 2019, *ApJ*, 883, L2
- Myers S. T. et al., 2003, *MNRAS*, 341, 1
- Napier K., Foord A., Gallo E., Ghisellini G., Hodges-Kluck E., Wu J., Haardt F., Ciardi B., 2020, *MNRAS*, 498, 1550
- Oh K. et al., 2018, *ApJS*, 235, 4
- Padovani P. et al., 2017, *A&AR*, 25, 2
- Paliya V. S. et al., 2019, *ApJ*, 881, 154
- Paliya V. S., Ajello M., Cao H. M., Giroletti M., Kaur A., Madejski G., Lott B., Hartmann D., 2020a, *ApJ*, 897, 177
- Paliya V. S. et al., 2020b, *ApJ*, 903, L8
- Polletta M. et al., 2007, *ApJ*, 663, 81
- Ricci C. et al., 2017, *ApJS*, 233, 17
- Sbrarato T., Ghisellini G., Tagliaferri G., Foschini L., Nardini M., Tavecchio F., Gehrels N., 2015, *MNRAS*, 446, 2483
- Schmidt M., 1968, *ApJ*, 151, 393
- Schwartz D. et al., 2019, *Astron. Nachr.*, 340, 30
- Schwartz D. A. et al., 2020, *ApJ*, 904, 57
- Shen X., Hopkins P. F., Faucher-Giguère C.-A., Alexander D. M., Richards G. T., Ross N. P., Hickox R. C., 2020, *MNRAS*, 495, 3252
- Siemiginowska A., Stawarz Ł., Cheung C. C., Harris D. E., Sikora M., Aldcroft T. L., Bechtold J., 2007, *ApJ*, 657, 145
- Simionescu A. et al., 2016, *ApJ*, 816, L15
- Smirnov N., 1948, *Ann. Math. Statist.*, 19, 279
- Steffen A. T., Strateva I., Brandt W. N., Alexander D. M., Koekemoer A. M., Lehmer B. D., Schneider D. P., Vignali C., 2006, *AJ*, 131, 2826
- Tavecchio F., Maraschi L., Sambruna R. M., Urry C. M., 2000, *ApJ*, 544, L23
- Toda K., Fukazawa Y., Inoue Y., 2020, *ApJ*, 896, 172
- Wolf J. et al., 2021, *A&A*, 647, A5
- Worrall D. M., Birkinshaw M., Marshall H. L., Schwartz D. A., Siemiginowska A., Wardle J. F. C., 2020, *MNRAS*, 497, 988
- Wu J., Brandt W. N., Miller B. P., Garmire G. P., Schneider D. P., Vignali C., 2013, *ApJ*, 763, 109
- Zhu S. F., Brandt W. N., Wu J., Garmire G. P., Miller B. P., 2019, *MNRAS*, 482, 2016

APPENDIX A: GB6J1711 + 3830 X-RAY ANALYSIS

In this section, we report the X-ray analysis of the source: GB6J1711 + 3830. This is a $z = 4.0$ AGN (the optical spectrum is reported in C19) classified as a blazar candidate on the basis of its radio properties. This is the only object from Caccianiga et al. (2019) whose X-ray analysis was not included in Ighina et al. (2019) because it had not been observed at the time of publication; we discuss the analysis and its X-ray properties here. The dedicated 50 ks X-ray observation was carried out between 2020 October and November with the *Swift*-XRT telescope (Obs. ID: 3110834, P.I. Belladitta). We analysed it following the same procedure used for the rest of the C19 sample, that is, using the XSPEC (v12.11.1) package and considering a simple power law absorbed by the Galactic column density along the line of sight ($N_H = 4.07 \times 10^{20} \text{ cm}^{-2}$; HI4PI Collaboration 2016). Combining the results of this analysis with optical information from the Panoramic Survey Telescope and Rapid Response System ($m_i = 20.46 \pm 0.01$; Chambers et al. 2016) we also computed the rest-frame ratio between the X-ray (10 keV) and the

Table A1. Results of the X-ray analysis on GB6J1711 + 3830.

Γ	$f_{0.5-10 \text{ keV}}^a$	$L_{2-10 \text{ keV}}^b$	$\tilde{\alpha}_{ox}$	cstat / d.o.f.
$1.46^{+0.31}_{-0.31}$	$8.26^{+2.06}_{-1.62}$	$3.84^{+0.52}_{-0.57}$	$1.148^{+0.053}_{-0.043}$	77.7 / 66

Notes. Errors are reported at 90 per cent level of confidence.

^ain units of $10^{-14} \text{ erg s}^{-1} \text{ cm}^2$.

^bin units of $10^{45} \text{ erg s}^{-1}$.

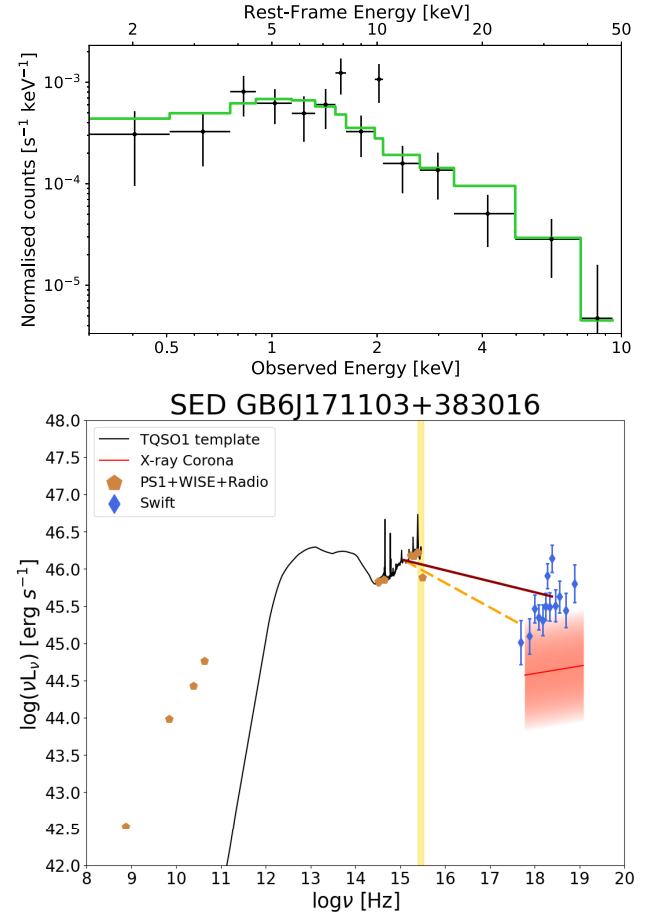


Figure A1. **Top:** X-ray spectrum of GB6J1711 + 3830 from the *Swift*-XRT dedicated observation modelled with a power law with only Galactic absorption (the solid green line). The data have been binned at 3σ significance for graphical purposes only. **Bottom:** Broad-band spectral energy distribution of GB6J1711 + 3830. The X-ray data from *Swift*-XRT are reported as the blue diamonds, while the radio and optical data (the brown pentagons) are described in the text. The black line is a template for the optical emission of quasars (Polletta et al. 2007), while the red line and the corresponding shaded region indicate the expected X-ray emission from the X-ray corona in a RQ AGN (Steffen et al. 2006).

UV (2500 Å) luminosities, the $\tilde{\alpha}_{ox}$ parameter⁶ (Ighina et al. 2019). Adopting the classification used for the rest of the C19 sample based on the shape ($\Gamma < 1.8$) and the relative X-ray luminosity compared to the optical one ($\tilde{\alpha}_{ox} < 1.355$), we consider GB6J1711 + 3830 as a bona fide blazar in this work. We report in Table A1 the results of the analysis and in Fig. A1 the observed X-ray spectrum (top panel) and its rest-frame multiwavelength SED (bottom panel).

$${}^6\tilde{\alpha}_{ox} = -0.303 \log \frac{L_{10 \text{ keV}}}{L_{2500 \text{ Å}}}.$$

Optical data are from PanSTARRS and radio data from the Giant Metrewave Radio Telescope all-sky survey (150 MHz; Intema et al. 2017), NVSS (1.4 GHz), the Green-Bank Survey (5 GHz; Gregory et al. 1996), and the The Karl G. Jansky Very Large Array (8.4 GHz). The red-shaded region represents the expected X-ray luminosity of a RQ AGN considering the L_{UV} – L_X relation, and its 1σ uncertainty, reported in Steffen et al. (2006), whereas the yellow column indicates the region with a significant dropout of the luminosity caused by the Lyman absorption (912–1216 Å). The slopes of the solid red and

orange-dashed lines are given by $1-\tilde{\alpha}_{ox}$ and $1-\alpha_{ox}$,⁷ respectively. The optical-IR template in black is taken from the SWIRE template library (Polletta et al. 2007).

$$^7\alpha_{ox} = -0.384 \log \frac{L_{2\text{keV}}}{L_{2500\text{Å}}}.$$

This paper has been typeset from a \LaTeX file prepared by the author.